

# Globular cluster populations and the kinematical fingerprints of minor mergers

N. C. Amorisco<sup>1,2\*</sup>

<sup>1</sup>*Institute for Theory and Computation, Harvard-Smithsonian Center for Astrophysics, 60 Garden St., MS-51, Cambridge, MA 02138, USA*

<sup>2</sup>*Max Planck Institute for Astrophysics, Karl-Schwarzschild-Strasse 1, 85748 Garching, Germany*

12 November 2021

## ABSTRACT

We use Monte Carlo  $\Lambda$ CDM assembly histories, minor-merger N-body simulations and empirical relations between halo mass and the globular cluster (GC) abundance to study the kinematical properties of halo GCs in massive galaxies, with  $M_{\text{vir}}(z=0) = 10^{13.5} M_{\odot}$ . We show that, in contrast with the accreted stellar halo, the accretion events contributing to the assembly of the halo populations of red and blue GCs are increasingly biased towards low satellite-to-host virial mass ratios. As a direct consequence, and in agreement with observations, our cosmologically accreted blue GC populations are systematically more extended and have higher velocity dispersions than for red GCs, due to the reduced efficiency of dynamical friction on minor mergers. For the same reason, the half-number radii of both GC populations are found to correlate with halo assembly history. GC line-of-sight velocity distributions featuring negative values of the kurtosis  $\kappa$ , as recently observed, are ubiquitous in our models. Therefore,  $\kappa < 0$  is not at odds with an accretion scenario, and in fact a fingerprint of the important contribution of minor mergers. However, our populations of accreted GCs remain mostly radially biased, with profiles of the anisotropy parameter  $\beta$  that are mildly radial in the center ( $\beta(r < 10 \text{ kpc}) \sim 0.2$ ) and strongly radially anisotropic at large galactocentric distances ( $\beta(r > 30 \text{ kpc}) \gtrsim 0.6$ ).

**Key words:** galaxies: structure — galaxies: star clusters — galaxies: kinematics and dynamics — galaxies: formation

## 1 INTRODUCTION

Globular clusters (GCs) are valuable tracers of the kinematics and assembly of galaxies. Compact and bright, they are observable in distant galaxies as well as at large distances from the galaxy centre. As such, GCs have had a fundamental role in studies aimed to probing the dark matter distribution in massive early type galaxies (e.g., Grillmair et al. 1994; Saglia et al. 2000; Romanowsky & Kochanek 2001; Schuberth et al. 2012; Agnello et al. 2014; Napolitano et al. 2014; Pota et al. 2015; Zhu et al. 2016, and references therein) or to constraining their assembly history (e.g., Zepf & Ashman 1993; Forbes et al. 1997; Côté et al. 1998; Brodie & Strader 2006; Li & Gnedin 2014; Mistani et al. 2016, among many others).

Intriguingly, GC populations appear to have strong ties to dark matter haloes. While the efficiency of haloes in forming galaxies is a markedly non-monotonic function of halo mass (e.g., Guo et al. 2010; Moster et al. 2010; Behroozi et al. 2013), the GC abundance – or the total stellar mass

in GCs – appears to be roughly proportional to halo mass (e.g., Blakeslee et al. 1997; Spitler & Forbes 2009; Georgiev et al. 2010; Hudson et al. 2014; Harris et al. 2017). Such an approximately linear relation extends to low-mass haloes, so that, within a  $\Lambda$ CDM framework, it directly follows that a considerable fraction of GCs in massive galaxies have not been formed within the main progenitor, but rather they have been accumulated through hierarchical merging (e.g., White & Frenk 1991). In fact, a close to linear relation works well with the scenario in which most GCs, and especially metal poor GCs, form at high redshift (e.g., Peebles 1984; Ricotti 2002; Kravtsov & Gnedin 2005; Brodie & Strader 2006, and references therein), as hierarchical assembly would approximately preserve this linearity.

The kinematics of accreted stellar populations deposited in the halo of galaxies through hierarchical accretion has been studied in detail, with particular attention to the case of Milky Way (MW) mass galaxies (e.g., Dekel et al. 2005; Abadi et al. 2006; Moore et al. 2006; Oñorbe et al. 2007; Cooper et al. 2010). A general result of these analyses is that radial orbits are dominant, and that the deposited stellar material is therefore characterised by a marked ra-

\* E-mail: nicola.amorisco@cfa.harvard.edu

dial anisotropy,  $\beta > 0$ , where  $\beta(r)$  is the classical anisotropy parameter

$$\beta(r) = 1 - \frac{\sigma_t^2(r)}{2\sigma_r^2(r)}, \quad (1)$$

with  $\sigma_t$  and  $\sigma_r$  being respectively the tangential and radial stellar velocity dispersions. Given the common accretion origin, and the apparent generality of this finding, it would seem only natural that the halo population of accreted GCs should also share this property.

However, the recent increase in both size and quality of GC spectroscopic datasets (e.g., [Pota et al. 2013](#); [Zhang et al. 2015](#); [Forbes et al. 2017](#)) have sparked a question on whether the simple picture above may be incomplete. For instance, following the described line of thought, the line-of-sight velocity distribution (LOSVD) of accreted GCs should be characterised by a positive kurtosis, as generally expected for populations with orbital distributions that have a strong radial bias (e.g., [Gerhard 1993](#); [van der Marel & Franx 1993](#)). As a first approximation, the kurtosis  $\kappa$

$$\kappa(R) = \frac{1}{\sigma_{\text{LOS}}^4(R)} \int dv [\text{LOSVD}(v, R) - \mu(R)]^4, \quad (2)$$

quantifies departures from Gaussianity in the LOSVD that are symmetric with respect to the mean  $\mu$ . Here  $R$  is the projected galactocentric radius and  $\sigma_{\text{LOS}}(R)$  the LOS velocity dispersion. Radially biased populations are characterised by LOSVDs with heavy tails and a sharp central peak, corresponding to  $\kappa > 0$  (see e.g., [Amorisco & Evans 2012](#)). Instead, [Pota et al. \(2013\)](#) have shown that both red and blue GC populations often display LOSVDs with kurtosis  $\kappa \sim 0$ , suggesting orbits that are close to isotropic. Positive values of  $\kappa$  are often observed at large galactocentric radii, but negative values of  $\kappa$  are common for both red and blue GCs in the galaxy's central regions, as also confirmed by [Zhang et al. \(2015\)](#). Taken at face value, these unexpected findings would suggest some degree of *tangential* anisotropy. If the generalisation from the kinematic properties of the stellar halo to those of the accreted GC populations is warranted, this would be at odds with the scenario in which a substantial fraction of all GCs are accreted.

In this paper, we show that there is in fact no contradiction between the observed negative values of the kurtosis in the LOSVDs of halo GCs and the scenario in which most of them have an accretion origin. We show that negative values of the kurtosis are expected within a  $\Lambda$ CDM framework when minor mergers are the dominant contributing channel of an accreted population, without the need to invoke additional physical processes. Due to the approximate linearity of the relation between halo mass and GC abundance, and in opposition to stellar haloes, minor mergers are indeed dominant in assembling the accreted populations of GCs, especially for blue metal poor GCs.

In Section 2 we use  $\Lambda$ CDM assembly histories to show how stellar and GC haloes have systematically different mean progenitors. Section 3 concentrates on the kinematic properties of material deposited in the accreted halo by satellites with different properties. Section 4 builds toy models for the populations of cosmologically accreted GCs, and focuses on their intrinsic and projected kinematic properties. Section 5 discusses results and lays out the Conclusions.

## 2 THE PROGENITORS OF STELLAR AND GC HALOES

Based on the merger rates of dark matter halos in the Millennium simulation ([Fakhouri et al. 2010](#)), we construct two sets of Monte Carlo  $\Lambda$ CDM assembly histories, one for haloes of MW-like virial mass,  $\log M_{\text{host}}(z=0)/M_{\odot} = 12.3$ , and one for haloes with virial mass  $\log M_{\text{host}}(z=0)/M_{\odot} = 13.5$ , representative of a massive central galaxy. Each set explores  $10^3$  individual halo assembly histories. For each host halo, we keep track of all accretion events onto the main progenitor for satellites with virial mass  $\log M_{\text{sat}}/M_{\odot} > 7$  at the time of accretion, since  $z = 6$ . These accreted satellites contribute stars to the accreted halo population of the host according to a standard stellar-to-halo mass relation (SHMR). In particular, we adopt a mean relation as presented by [Garrison-Kimmel et al. \(2014\)](#), and assume a Gaussian scatter of 0.3 dex. For simplicity, both mean relation and scatter are assumed to be independent of redshift. The resulting SHMR is displayed with a black line in the left panel of Fig. 1.

Accreted satellites also contribute to the accreted GC population of the host. We track red and blue GCs separately and assume that the GC population of each satellite is a function of the halo mass at accretion. In particular, we adopt mean relations as measured by [Harris et al. \(2015\)](#):

$$\begin{cases} \log N_{GC,red} &= 1.8 + 1.21 (\log M_{\text{sat}} - 12.2) \\ \log N_{GC,blue} &= 2.0 + 0.96 (\log M_{\text{sat}} - 12.2) \end{cases}. \quad (3)$$

With a log-log slope of 0.96, the abundance of blue GCs is approximately proportional to the virial mass of the satellite, while the abundance in red GCs is slightly steeper, for a log-log slope of 1.21. We take that, in addition to Poisson noise, the intrinsic scatter around these mean relations is of 0.3 dex. The left panel of Fig. 1 compares GC abundances and the SHMR (the shading shows the different 1-sigma regions). It is worth noticing that the empirical relations (3) have been measured at  $z = 0$ , while we require estimates of the GC abundance of satellites at the time of accretion. In absence of measurements for the same relations as a function of redshift, we take that the abundances (3) are independent of redshift. This is the same simplifying assumption made for the SHMR. Though not ideal, this can be considered conservative here. With respect to a model in which GCs are formed at high redshift with an abundance that is proportional to halo mass *at that time* (see e.g., [Boylan-Kolchin 2017](#)), the present model implies an underestimation of the role of minor mergers, as massive haloes assemble more recently.

Given the set of minimal hypotheses above, Figure 1 shows the cumulative fraction  $f$  of accreted halo populations, in stars and GCs, contributed by satellites with different satellite-to-host virial mass ratio at accretion (VMR),  $\log M_{\text{sat}}/M_{\text{host}}$ . The middle panel refers to our set of MW-like haloes. The right panel to our massive haloes with  $M_{\text{vir}}(z=0) = 10^{13.5} M_{\odot}$ . Thick lines show median relations, the shaded regions extend between the {5, 25, 75, 95}% quantiles. Fig. 1 shows very clearly that the average progenitor satellite of stellar halo and accreted GC populations are remarkably different.

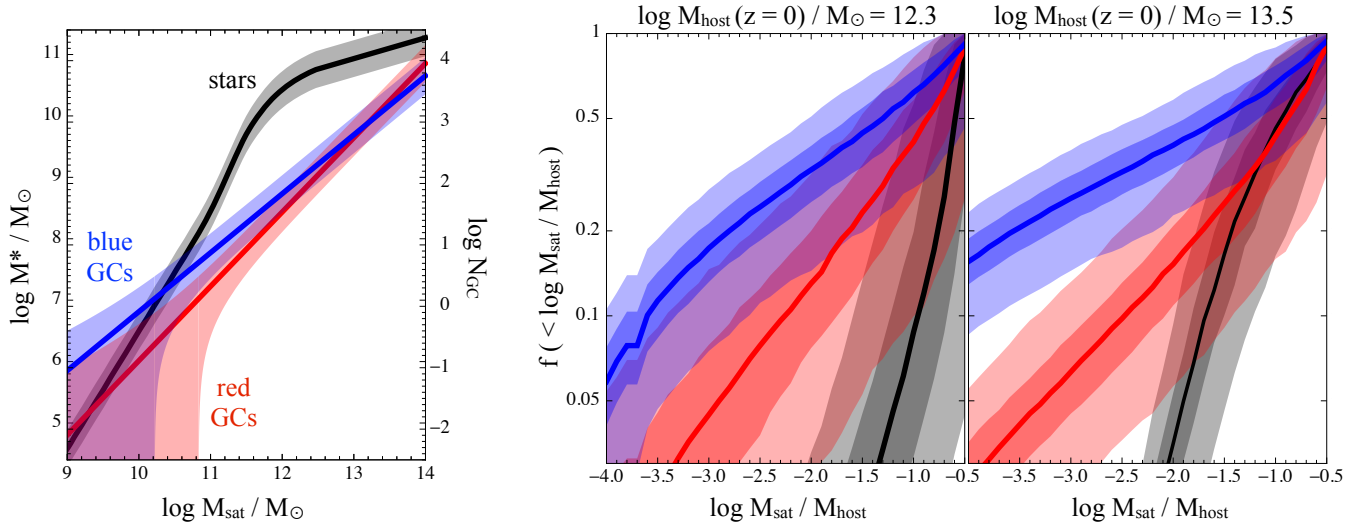


**Figure 1.** Left panel: the relation between halo mass of the contributing satellites and the contributed stellar mass (in black), red GCs (in red), blue GCs (in blue). The shading identifies the 1-sigma regions around the mean model relations (including both intrinsic and Poisson scatter for GCs). Middle and right panels: cumulative contributions to the accreted stellar and GC populations, as a function of the virial mass ratio at accretion,  $\log M_{\text{sat}}/M_{\text{host}}$ . Thick lines identify medians, shaded regions extend between the  $\{5, 25, 75, 95\}$ % quantiles, over a sample of  $10^3$  halo assembly histories. The middle panel refers to the halo of a Milky Way-like galaxy  $\log M_{\text{host}}(z=0)/M_{\odot} = 12.3$ . The right panel to a massive elliptical galaxy  $\log M_{\text{host}}(z=0)/M_{\odot} = 13.5$ .

## 2.1 MW-like haloes

As shown in the middle panel of Fig. 1, the contribution of low mass satellites to the accreted stellar halo of MW like galaxies drops quickly at  $\log M_{\text{sat}}/M_{\text{host}} \lesssim -1$ . This is a well-known result (e.g., Bullock & Johnston 2005; Sales et al. 2007; Cooper et al. 2010; Deason et al. 2016; Amorisco 2017a) and a direct consequence of the steepness of the SHMR at virial masses  $\log M_{\text{sat}}/M_{\odot} \lesssim 12$ , with a log-log slope of  $\sim 1.9$  (e.g., Garrison-Kimmel et al. 2014, 2017; Jethwa et al. 2018). As shown by the first panel of Fig. 1, the relations (3) prescribe GC abundances that are considerably less steep with halo mass, resulting in much higher fractions of accreted GCs being contributed by satellites with low VMR. For example, accretion events with  $\log M_{\text{sat}}/M_{\text{host}} < 1/50$  contribute between 30 and 48% (respectively 25 and 75% quantiles) of the blue GCs in MW-like galaxies. This is in stark contrast with the  $<3\%$  contributed to the stellar halo by the same satellites (75% quantile).

It is interesting to note that, in MW mass galaxies, the median distribution of VMRs of satellites contributing to the stellar halo, to the accreted population of red GCs and to the accreted population of blue GCs are all systematically different from each other. As already mentioned, the stellar halo is dominated by high VMR accretion events. Minor mergers become increasingly important for red and blue GCs. As we will show in the following, this implies that the spatial distribution and kinematic properties of these three halo populations should be expected to be different.

In this simple model, haloes with  $\log M_{\text{host}}(z=0)/M_{\odot} = 12.3$  accrete a total of between 149 and 196 blue GCs, and 31 to 49 red GCs (25 and 75% quantiles for both populations). Given the simplistic hypotheses on which they are based, these figures should be taken as qualitative estimates. However, it is interesting to notice that the simplest possible combination of physical ingredients, i.e.  $\Lambda$ CDM as-

sembly histories and the measured GC abundances (3) appear to produce  $z=0$  GC populations that compare favorably with expectations. Both total GC abundance (see e.g., Harris et al. 2017) and ratio between red and blue GC populations (Harris et al. 2015) are roughly reproduced.

## 2.2 Massive haloes

The case of haloes with virial mass  $\log M_{\text{host}}(z=0)/M_{\odot} = 13.5$  is illustrated in the rightmost panel of Fig. 1. The relation between the abundance of blue GCs and halo mass is the least steep, so the fractional contribution of minor mergers is highest for blue GCs, as for the case of MW mass haloes. Between 39 and 55% of blue GCs (25 and 75% quantiles) are contributed by satellites with  $\log M_{\text{sat}}/M_{\text{host}} < 1/50$ .

Fig. 1 also shows that the contribution of low mass satellites to the accreted stellar halo of high mass galaxies is also higher than in the case of MW-like galaxies. This is a consequence of the break in the SHMR at MW masses, and also a well known result (e.g., Purcell et al. 2007; Naab et al. 2007; Cooper et al. 2013; Pillepich et al. 2014). What is especially interesting here is that the cumulative fraction of accreted material in the two halo populations track each other down to  $\log M_{\text{sat}}/M_{\text{host}} \sim -1.2$ , corresponding to approximately 65% of either populations. This implies that a majority of the material in the accreted stellar halo and in the accreted population of red GCs have similar progenitors in massive galaxies. This provides a qualitative justification to the finding that red GCs often trace the distribution of stars in massive galaxies not just in the center, but also out to large galactocentric distances (e.g., Strader et al. 2011; Pota et al. 2013; Agnello et al. 2014), where both stellar and GCs populations are expected to be dominated by accreted material. Note however, that the scatter in the distributions of VMRs is significant for both populations, suggesting that this similarity may be loose in some systems. For complete-

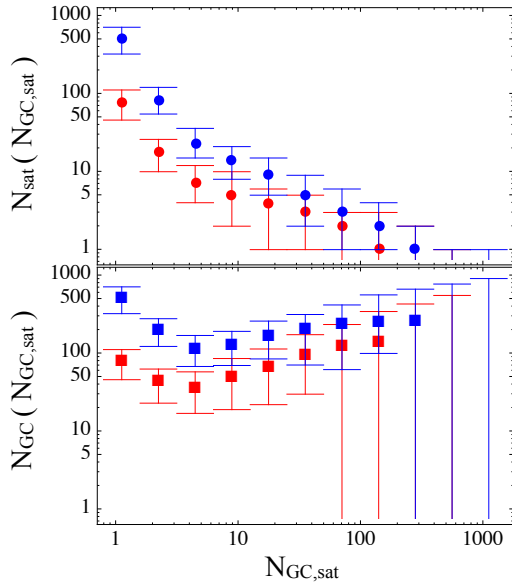


**Figure 2.** Upper panel: the total number of accreted satellites  $N_{\text{sat}}$  as a function of the number of contributed GCs,  $N_{GC,\text{sat}}$  GCs. Lower panel: the total number of GCs accreted from satellites contributing  $N_{GC,\text{sat}}$  GCs each. Red and blue points refer to the populations of red and blue GCs. Points indicate median values over a sample of  $10^3$  halo assembly histories, error bars extend between the 10 and 90% quantiles.

ness, the total number of accreted blue GCs estimated by this simple model is of between 2350 and 2950, and of between 850 and 1250 for red GCs (25 and 75% for both populations), again in rough agreement with the expectation for this halo mass.

Figure 2 concentrates on the size the different contributions to the accreted GC populations:  $N_{GC,\text{sat}}$  on the  $x$  axis is the number of GCs contributed by an individual satellite. The top panel shows a demography of all contributions in terms of the number of accreted satellites that contribute  $N_{GC,\text{sat}}$  GCs, since  $z = 6$ . Points indicate medians, while the error bars extend between 10 and 90% quantiles of the distribution. Satellites that contribute  $>100$  GCs are rare, for both blue and red GCs. Due to preponderance of low mass accretion events, in these simple models, there are on average more satellites contributing a single GC than satellites contributing  $N_{GC,\text{sat}} > 1$ . This is mirrored in the lower panel, which shows the total number of GCs accreted in a contribution of size  $N_{GC,\text{sat}}$ . Here the Poisson noise in the assembly histories is especially evident: high VMR mergers (e.g.,  $M_{\text{sat}}/M_{\text{host}} > 0.5$ ) are rare, but may contribute a large fraction of all GCs, introducing significant stochasticity. The number of GCs contributed individually or as part of small groups shows less scatter, and is consistently high in all assembly histories.

### 3 VIRIAL MASS RATIOS AND KINEMATICS

Amorisco (2017b) (hereafter NA17) has shown that, for  $\Lambda$ CDM accretion events, the satellite-to-host VMR is the parameter that drives the kinematical properties of any accreted material. The efficiency of dynamical friction in-

creases with VMR, so that massive satellites manage to sink deeper in the central regions of the host, and depositing their contributions there. Instead, dynamical friction has little effect on the orbits of low mass satellites, especially for VMRs  $M_{\text{sat}}/M_{\text{host}} \lesssim 1/50$ . As a result, the VMR of the mean progenitor contributing material at radius  $r$  is a function of radius, with minor mergers contributing preferentially at large galactocentric distances (see also Rodriguez-Gomez et al. 2016).

While sinking, massive satellites see their orbits become increasingly radial, to the point that essentially all memory of the orbital properties at infall is lost for  $M_{\text{sat}}/M_{\text{host}} \gtrsim 1/20$ . Consequently, the material deposited by massive satellites has a strong radial bias. On the other hand, minor mergers are substantially less affected, and preserve a larger fraction of their orbital angular momentum. As the mean orbital circularity of cosmological accretions is  $j \sim 0.5$  (e.g., Benson 2005; Wetzel 2011; Jiang et al. 2015, here  $j$  is the ratio of the orbital angular momentum  $J$  to the maximum angular momentum for the same orbital energy,  $J_{\text{circ}}(E)$ ), on average, the material contributed by low mass satellites has a considerable angular velocity.

We take the isolated minor merger N-body simulations presented in NA17. These consider the mergers of two idealised spherical, non-rotating dark matter haloes with Navarro-Frenk-White density profiles (NFW, Navarro et al. 1997). The suite presented in NA17 considers a range of different structural and orbital parameters, and we refer the reader to that work for more details. For this paper, we use the runs corresponding to mean values for the satellite-to-host density contrast (i.e. mean dark halo concentration parameters for both host and satellite haloes), a circularity at infall of  $j = 0.5$ , and different values of the satellite-to-host VMR:  $M_{\text{sat}}/M_{\text{host}} \in \{-2.1, -1.7, -1.3, -0.9, -0.5\}$ . As discussed in NA17, the limits of this approach are analogous to those of a the so called ‘particle-tagging’ technique (e.g., Bullock et al. 2001; Bullock & Johnston 2005; Cooper et al. 2010, 2013; Ramos-Almendares et al. 2017), which are extensively discussed in the literature (see e.g., Cooper et al. 2010; Bailin et al. 2014; Cooper et al. 2017, NA17). Here we use a tagging fraction of  $f_{\text{tag}} = 8\%$ .

The left panel of Fig. 3 shows the distribution of orbital velocities  $v_\varphi$  of material contributed by satellites with different VMR. The angle  $\varphi$  is the angle in the satellite’s orbital plane,  $r_s$  is the scale radius of the host NFW halo and  $v_{\text{max}}$  is its maximum circular velocity. The shaded regions extend between the 10 and 90% quantiles of the distribution and the colour-coding is as in the legend at the top. The kinematical properties of the accreted material display a clear gradient with VMR. Material contributed by massive satellites does not preserve coherent rotation, and is scattered in an approximately symmetric way with respect to the direction of the satellite’s orbital motion at infall, i.e. with respect to  $v_\varphi = 0$ . With decreasing VMR, more and more angular momentum is retained and the contributed material traces more closely the infall orbit itself, which is shown as a dash-dotted line.

The middle and right panels in the same Figure show the fraction of the total kinetic energy  $K$  associated with rotating motion in the  $\varphi$  direction,  $K_\varphi/K$ , together with the fraction in radial motion  $K_r/K$ . Lines display medians over the contributed material. The dash-dotted lines indicate the

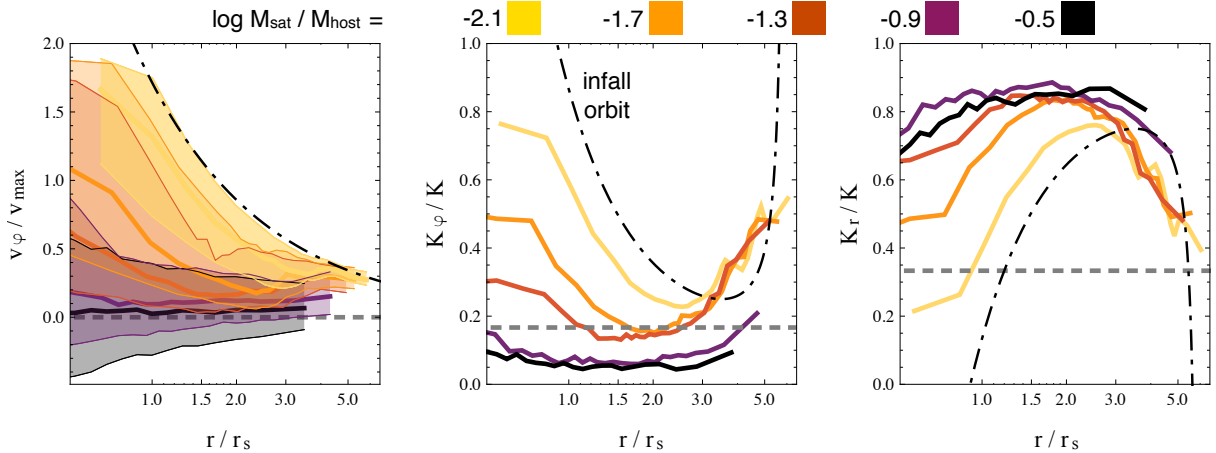


**Figure 3.** Kinematical properties of individual contributions from satellites with different virial mass ratio at accretion, color-coded as in the legend at the top. The shaded regions in the right panel extend between the 10 and 90% quantiles of the distribution of rotational velocities of particles contributed by individual satellites. The middle panel shows the fraction of the total kinetic energy in ordered rotation  $K_\phi/K$ , the right panel the fraction in radial motion  $K_r/K$ . In all panels the dot-dashed black line describes the common infall orbit of all satellites, while the grey dashed line displays the expectation for a non rotating, isotropic population (after averaging over radius).

infall orbit. Horizontal dashed lines show the expectation for the mean fraction of kinetic energy of a non rotating population with isotropic orbital distribution. Although these lines are not directly comparable with the coloured curves due to the additional averaging over radius, both gradual increase in tangential motion with decreasing VMR and increase in radial bias are quite clear.

### 3.1 LOSVDs and kurtosis

The kinematic properties illustrated in the previous Section characterise the material deposited by individual satellites. Here we wish to focus on the LOSVDs obtained by superposing the contributions of multiple satellites. For the moment we ignore the cosmological setting, which will be introduced in Section 4, and, for each VMR as in Fig. 3, we superpose a large number of contributions from satellites infalling from random directions. Figure 4 shows the resulting LOSVDs: different columns identify different mass ratios as indicated at the top, while different rows are for different projected circular annuli. For context, assuming mean concentration parameters (e.g., Ludlow et al. 2014), the scale radius  $r_s$  of an NFW halo with  $\log M_{\text{host}}(z=0)/M_\odot = 13.5$  is  $r_s \sim 70$  kpc ( $r_s \sim 100$  kpc) at  $z=1$  ( $z=0$ ). All LOSVDs are displayed in terms of the normalised LOS velocity  $v_{\text{LOS}}/\sigma_{\text{LOS}}$ , where  $\sigma_{\text{LOS}}$  is calculated in the same radial interval. Profiles are colour-coded according to the value of their kurtosis  $\kappa$ , which is also displayed at the bottom of each panel. Green colours identify negative values of  $\kappa$ , while LOSVDs coloured in shades of pink have  $\kappa > 0$ . A diagonal colour divide is evident: negative values of the kurtosis are common for low VMRs and closer to the centre of the host. Positive values of the kurtosis become prevalent for increasing VMRs and at larger radii.

This qualitatively shows that negative values of  $\kappa$  have their origin in the contribution of minor mergers. In particular, markedly double peaked LOSVDs are common in the upper-left corner, resulting in negative values of  $\kappa$ . As

showed in the previous Section, material contributed by minor mergers follows quite closely the progenitor’s orbit, with high angular velocity. These double peaks are then caused by the superposition of individual sub-populations rotating with high angular velocities and random orientation. With increasing VMR, the degree of tangential motion in the contribution of each single satellites decreases, causing the double peaks to disappear and leave room to LOSVDs with heavy tails and sharper central peaks, typical of material moving on radially biased orbits.

The trend of the kurtosis  $\kappa$  with radius appear similar across different VMRs: i)  $\kappa(R)$  is increasing at small radii; ii) reaches a maximum that depends on VMR at a radius that decreases with VMR; then, at larger radii, iii)  $\kappa(R)$  appears to decrease. This common behaviour tracks orbital structure. At small and large radii most contributed particles approach respectively pericenter and apocenter, making double peaks more pronounced and lowering the value of the kurtosis. Due to dynamical friction, the radius of these turnaround points increases with decreasing VMR. Finally, as massive satellites shed material filling much larger phase space volumes, radial gradients in  $\kappa(R)$  are less pronounced for high VMRs.

In fact, the values of  $\kappa < 0$  seen in the top-left of Fig. 4 would likely be considered extreme in the framework of distribution function based dynamical modelling (e.g., Gerhard 1991, 1993; van der Marel & Franx 1993; Carollo et al. 1995; Bertin et al. 1997). The reason for the corresponding sharp double peaks is twofold. First, each of the populations of Fig. 4 are composed of multiple contributions with identical distributions of pericenters and apocenters. This is illustrative, but artificial in a cosmological context, where satellites accreted at different redshift deposit material at different radii around the host (e.g., Bullock & Johnston 2005; Cooper et al. 2010, NA17). Second, the phase space distribution of halo populations contributed by minor mergers are quite different from those suited for the modelling of the main stellar body of galaxies. The latter are usually

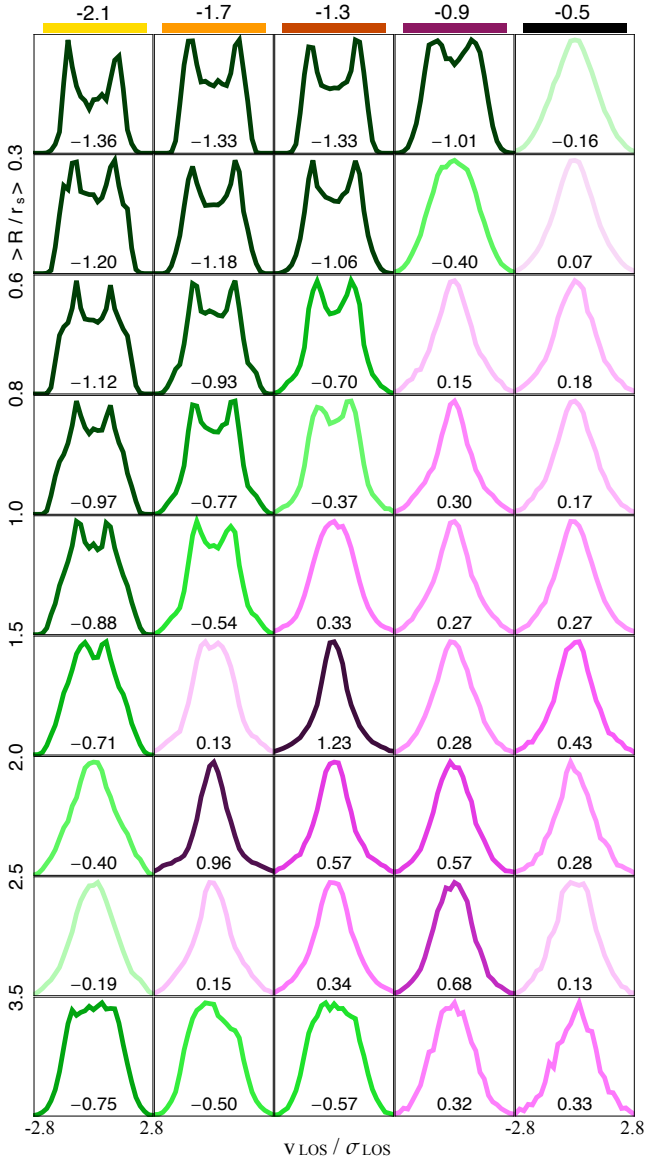


**Figure 4.** Line-of-sight velocity distributions for accreted populations contributed by satellites with identical satellite-to-host virial mass ratio. Each column refers to the virial mass ratio shown at the top. Different rows refer to different projected radial intervals. Individual line profiles are color-coded by the value of the kurtosis  $\kappa$ , which is indicated at the bottom of each panel.

required to generate monotonic density distributions, corresponding to a comparatively superior abundance of material moving with low 3D- and LOS- velocity, and therefore less pronounced double peaks. In turn, each minor merger contribution is significantly coherent in phase space, has a tight and non-monotonic distribution in energy, and a corresponding central density hole (see NA17).

#### 4 THE KINEMATICS OF COSMOLOGICALLY ACCRETED GC POPULATIONS

We now combine the  $\Lambda$ CDM assembly histories presented in Section 2 (a subset of 200) to the minor merger simulations introduced in Section 3, to construct toy models of the GC

populations cosmologically accreted by galaxies hosted by a halo with  $\log M_{\text{host}}(z=0)/M_{\odot} = 13.5$ . As done in Section 2, we track blue and red GCs accreted since  $z = 6$  separately, and assume that accreted satellites have deposited all of their GCs in the accreted halo of the host. We use N-body simulations with different VMRs to assign phase space coordinates to each GC at  $z = 0$ , sampling randomly among the most bound satellite’s particles, up to a tagging fraction of 8%. We assume accretion events are uncorrelated, and that satellites infall from random directions. To account for redshift evolution, we scale  $r_s$  and  $v_{\text{max}}$  to the values of the host NFW halo at the accretion redshift, using our assembly histories and a mean mass-concentration-redshift relation (e.g., Gao et al. 2008; Ludlow et al. 2014). We do not expect such a simplified model to provide a realistic description of the accreted GC populations. Rather, this investigation is aimed to explore to what degree the combination of the fundamental ingredients of the process of cosmological assembly (i.e.  $\Lambda$ CDM assembly histories, gravitational dynamics and observed GC abundances) can reproduce the observed kinematic properties and trends of GC halo populations.

#### 4.1 Edge-on kinematic maps

Figure 5 shows maps of the LOS kinematics of cosmologically accreted blue GCs. Different columns refer to subpopulations of GCs contributed across cosmic time by satellites with different VMRs, with values as in the legend at the top. The maps show median values across a set of 200 individual assembly histories. To visualise any rotation pattern, the displayed maps are edge-on projections, obtained by aligning the GC subpopulation of each individual halo according to its total angular momentum. The top row shows values of the LOS velocity  $v_{\text{LOS}}$ , the middle row shows velocity dispersion  $\sigma_{\text{LOS}}$ , the bottom row displays values of the kurtosis  $\kappa$ . Note that the radial scale is logarithmic, extending between 3 and 350 kpc as illustrated in the right-most panels.

First, we notice that the kurtosis  $\kappa$  displays very similar patterns as those identified in Section 3.1. i) Negative values of  $\kappa$  are dominant for material contributed by minor mergers. ii)  $\kappa$  increases with VMR and is higher at larger galactocentric radii. Both of these trends survive the ‘mixing’ process that accompany the cosmological setting, which causes material accreted at higher redshift to be deposited closer to the centre of the host halo.

Interestingly, the superposition of the contributions of multiple satellites may still result in coherent rotation, despite the assumption of uncorrelated infall directions. Negligible residual rotation is seen in the GC sub-population contributed by the satellites with the lowest or highest VMRs. In the former, the numerous individual contributions result in complete averaging. In the latter, each satellite deposits a non-rotating contribution, as shown in Fig. 3. At intermediate VMRs, however, material deposited by each individual satellite retains substantial rotation and the number of uncorrelated contributions is low enough that coherent rotation may survive. The mean rotation patterns seen in the averages of Fig. 5 are therefore dominated by the driving signal associated with the contribution of one single satellite, or to the fortuitous constructive superposition of a very small number of them. The significant scatter in the rela-

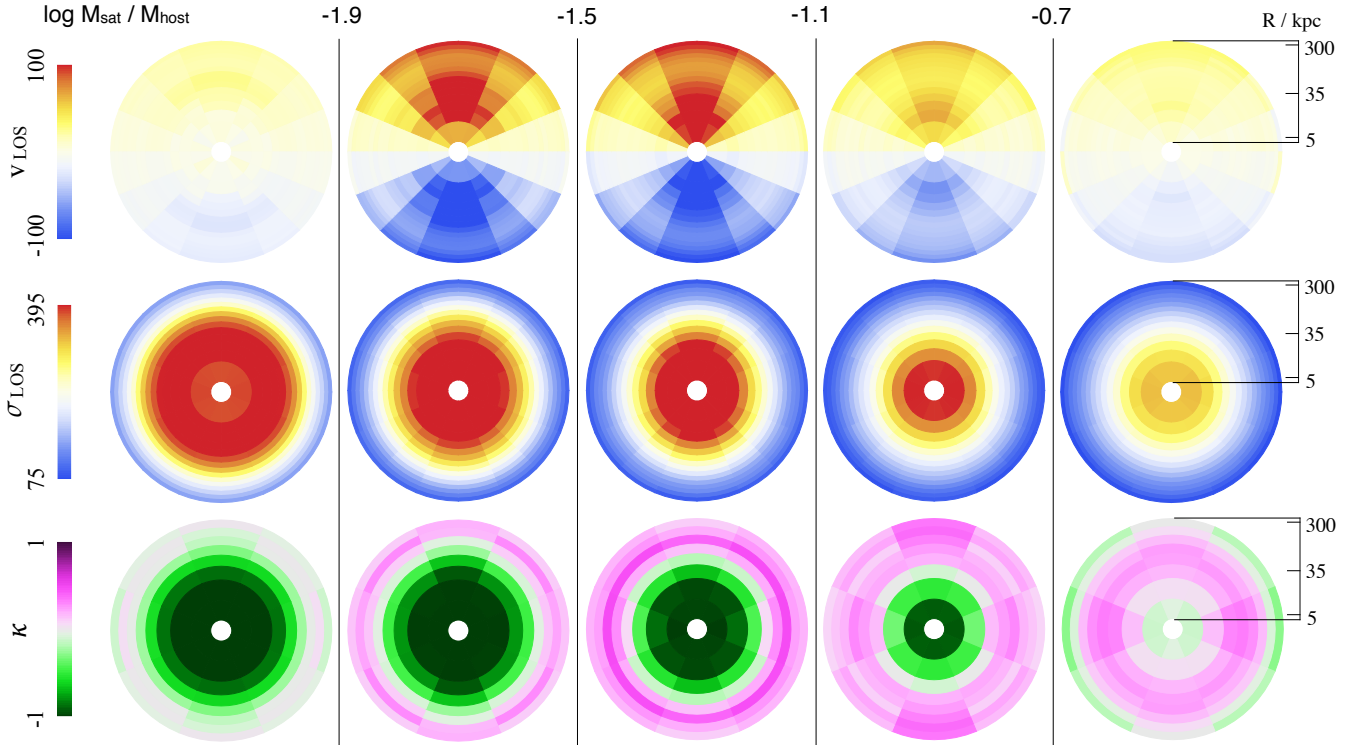


**Figure 5.** Edge-on projected kinematic maps for the accreted blue GC population (medians over 200 accretion histories), for a massive galaxy with  $\log M_{\text{host}}(z=0)/M_{\odot} = 13.5$ . Contributions of different satellites are grouped according to the value of the virial mass ratio at accretion, as indicated at the top of the figure.

tions (3) may also help individual contributions to dominate within their VMR bin. Note though, that any residual rotation in the two bins  $-1.9 < \log M_{\text{sat}}/M_{\text{host}} \leq -1.5$  and  $-1.5 < \log M_{\text{sat}}/M_{\text{host}} \leq -1.1$  will likely not add up in a constructive way, as the chance of aligning angular momentum vectors is low.

Values of the LOS velocity dispersions are clearly decreasing with VMR, which is a consequence of the increasing efficiency of dynamical friction. Material sinking to the center loses energy and has therefore lower velocities (see also NA17). Radial segregation has the same origin: Figure 6 displays the cumulative distribution functions (cdf) of the projected number counts of the different GC sub-populations. Thick lines are medians over the considered 200 assembly histories and the shaded regions extend between the 10 and 90% quantiles. The different sub-populations are radially ordered by VMR, and so is the magnitude of their scatters, which increase with VMR due to the increasing Poisson noise. Blue GCs accreted by satellites with  $\log M_{\text{sat}}/M_{\text{host}} > -0.7$  have a half-number radius  $R_h$  between 13 and 43 kpc (10 and 90% quantiles); between 135 and 185 kpc for  $\log M_{\text{sat}}/M_{\text{host}} < -1.9$ . The corresponding values for red GCs are very similar: the sub-populations of red and blue GCs defined by VMR of the contributing satellites are essentially indistinguishable. It is their different fractional contribution that causes any differences in the global kinematic properties of blue and red GCs, which we analyse in the following.

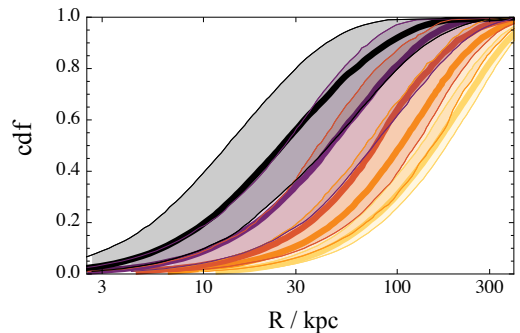


**Figure 6.** The cumulative distribution for the projected number counts of the sub-populations of cosmologically accreted GCs contributed by satellites with different mass ratios. Color-coding as in Fig. 4. The shading extends between the 10 and 90% quantiles over the studied set of 200 assembly histories.

#### 4.2 Mean projected kinematics

Figure 7 shows the LOS kinematic profiles of the full blue and red populations of accreted GCs. The sets of lines show the 25, 50 and 75% quantiles over our set of 200 assembly histories. Full lines include an averaging over inclinations (with respect to the angular momentum of the full blue GC accreted population), which we perform by using 20 random viewing angles for each individual halo. From left to right, columns display respectively: maximum rotational velocity  $v_{\text{LOS,max}}$ , velocity dispersion  $\sigma_{\text{LOS}}$ , kurtosis  $\kappa$  and cdf of the number counts.

We mimic the measurement procedures used with real

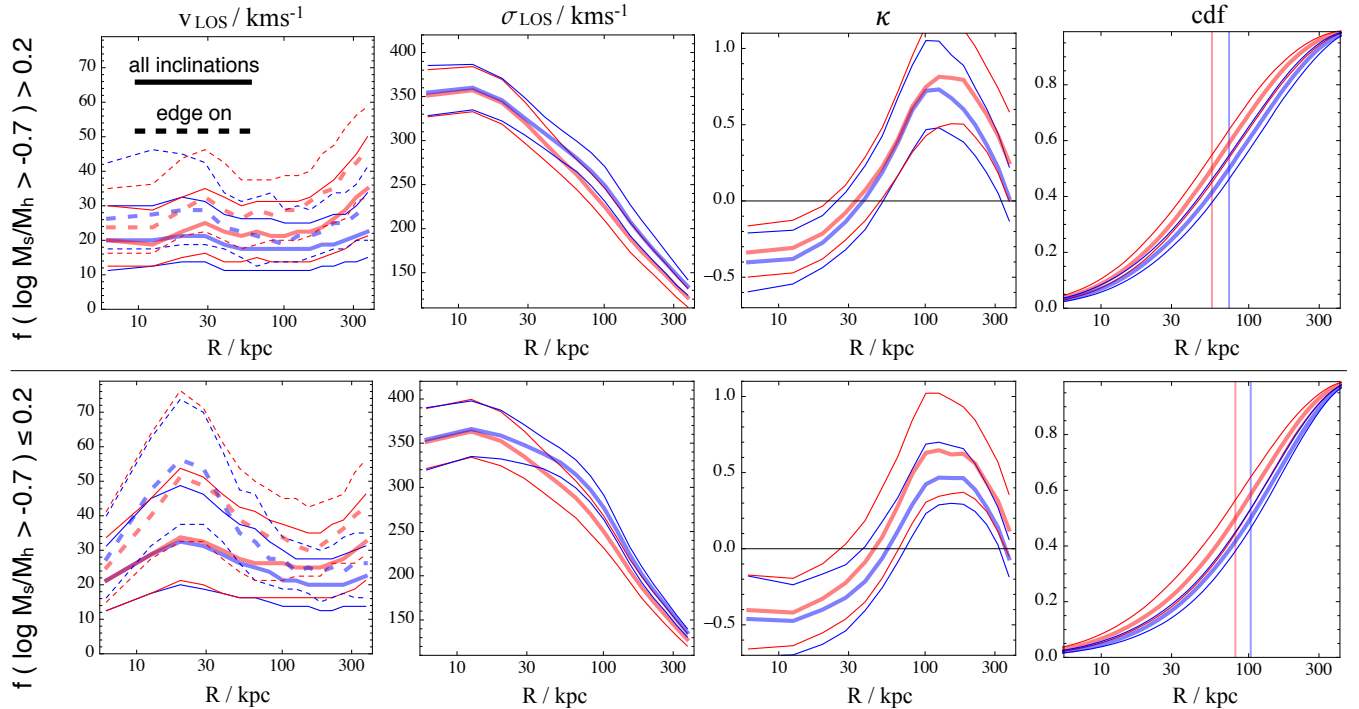


**Figure 7.** Mean projected kinematics for the cosmologically accreted blue and red GC populations, as a sum over all contributing satellites. The two rows of panels display the effect of different accretion histories: upper (lower) panels refer to assembly histories in which accretion events with  $\log M_{\text{sat}}/M_{\text{host}} > -0.7$  contribute  $> 20\%$  ( $\leq 20\%$ ) of all blue GCs, corresponding to a 50% of all studied assembly histories. In each panel, full lines average over viewing angles. Dashed lines in the left panel refer to viewing angles close to edge-on with respect to the total angular momentum of the accreted blue GCs (see text for details). In each row, the first panel shows the maximum line-of-sight rotational velocity, the second panel displays line-of-sight velocity dispersion, the third panel shows kurtosis, the fourth panel displays the cumulative distribution function for the projected number counts. In all cases, the sets of lines display the 25, 50 and 75% quantiles of the distribution, over different accretion histories and inclinations. The vertical lines in the right-most panel identify the half-count radius.

data (e.g., Pota et al. 2013): values of  $v_{\text{LOS,max}}$  are obtained by performing azimuthal fits in different radial bins, assuming a simple sinusoidal dependence,

$$v_{\text{LOS}}(R, \theta) = v_{\text{LOS,max}}(R) \cos(\theta - \theta_0). \quad (4)$$

As mentioned, this is repeated for 20 random viewing angles. Full lines display quantiles over the full set, dashed lines simulate a close to edge-on projection, by showing quantiles over the subset of those 10 angles that result in the highest values of  $v_{\text{LOS,max}}$ .

The two rows in Fig. 7 focus on a total of 100 different assembly histories each, dividing the full set according to the fraction of GCs contributed by satellites with  $\log M_{\text{sat}}/M_{\text{host}} > -0.7$ . As seen in Fig. 2, due to substantial averaging, the contribution of satellites with low VMR is quite stable over different assembly histories. Instead, accretion events with especially high VMR are highly stochastic, and may contribute a substantial fraction of the accreted GC population. For instance, in 50% of our assembly histories, the fraction of blue GCs contributed by satellites with  $\log M_{\text{sat}}/M_{\text{host}} > -0.7$  is  $< 0.21$ :  $f_{50}(\log M_{\text{sat}}/M_{\text{host}} > -0.7) = 21\%$ . However, the 95% quantile of the same fraction is a much higher  $f_{95}(\log M_{\text{sat}}/M_{\text{host}} > -0.7) = 57\%$ .

There are few aspects worth of notice.

- First of all, the accreted blue GCs are systematically more spatially extended than the red GCs, independently

of the accretion history. At the same time, the velocity dispersion of blue GCs stays consistently higher than that of red GCs. Both of these aspects are in agreement with observations and, in these models, are a natural consequence of the slightly different abundances prescribed by eqns (3). Blue GCs have a higher fractional contribution from minor mergers, and therefore more extended density distributions and higher velocity dispersions.

- The median radial profile of the kurtosis  $\kappa$  has a well defined shape, with preferentially negative values for both blue and red GCs within  $\sim 40$  kpc ( $\sim 50$  kpc in the bottom row, when minor mergers are dominant). Then,  $\kappa$  quickly increases towards positive values at larger radii. If the contribution of high VMR accretion events is substantial, higher values of  $\kappa$  are achieved (top row).

- Differences in the kinematical properties between the bottom and top row are systematic, but limited with respect to the scatters introduced by the details in the assembly histories. Residual rotation is stronger when minor mergers are dominant, and the velocity dispersion of both populations is consistently higher.

- Instead, the most noticeable difference between the bottom and top rows is in the spatial distributions. Vertical lines in the rightmost panels indicate half-count radii, which are significantly larger when the contribution of minor mergers is higher. It is difficult to make a direct comparison between these predicted sizes and measured values, mainly because



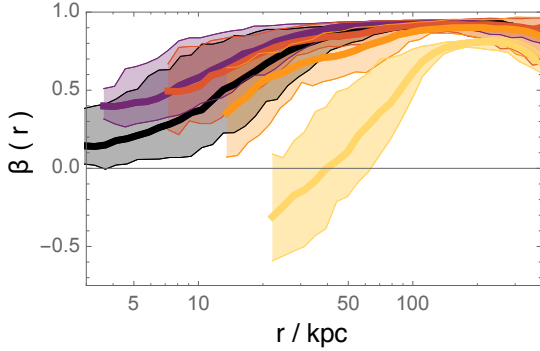


**Figure 8.** Profiles of the anisotropy parameter  $\beta(r)$  for the GC sub-populations as in Fig. 5 and 6. Lines indicate median values and the shading extends between the 10 and 90% quantiles over the studied set of 200 assembly histories. Colour-coding as in Fig. 4 and 6.

these models cannot account for any *in situ* GC population. However, it is reassuring that half-count radii compare well with observations for this halo mass (e.g., Forbes 2017; Hudson & Robison 2017), and promising that size appears to relate well with assembly history.

Finally, we note that rotation patterns in the GC populations of individual haloes are often twisted, i.e. the position angle  $\theta_0(R)$  as defined in eqn. (4) varies significantly with radius. This is the case for both blue and red GC populations. At the same time, red and blue GCs often have different kinematic position angles. This is a consequence of the stochastic nature of residual rotation in these simple models (see also e.g., Moody et al. 2014). As mentioned in Section 4.1, coherent rotation is driven by the contributions of satellites with intermediate VMR and survives only in the absence of efficient averaging. Due to both intrinsic and Poisson noise on the relations (3), it is not unlikely that the rotation signal of blue and red GC populations is dominated by the contribution of different satellites, with likely misaligned angular momentum vectors.

### 4.3 Orbital anisotropy

We have shown that negative values of the kurtosis are a natural product of the residual tangential motion of the contributions of minor mergers and that they are ubiquitous in the central regions for the accreted population of GCs. However, so far we have not directly addressed actual orbital structure. Figure 8 shows the anisotropy profile  $\beta(r)$  of the sub-populations of the accreted blue GCs defined by VMR of the parent satellite, as in Figs. 5 and 6 (same colour-coding). Thick lines show medians over our 200 assembly histories, shaded regions extend between the 5 and 95% of the distribution.

For all VMRs, anisotropy profiles increase towards large radii, with very high values of  $\beta$  reached at  $r \gtrsim 100$  kpc. Due to the segregation induced by dynamical friction, the profiles relevant to low VMRs do not extend to the very central regions of the host, where not enough GCs are contributed. However, it is clear that the anisotropy at  $r \lesssim 20$  kpc is different for different VMRs, and especially so for the contribution of satellites with  $\log M_{\text{sat}}/M_{\text{host}} < -1.9$ . The

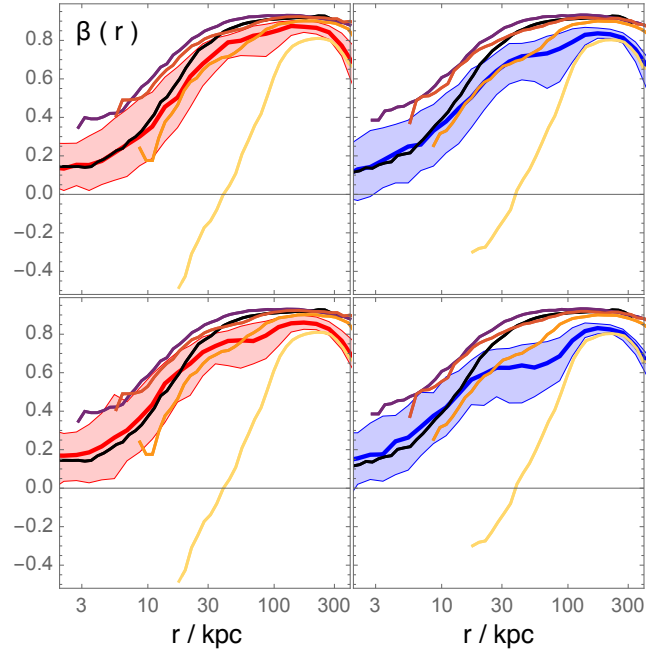


**Figure 9.** The anisotropy profiles of the cosmologically accreted red (left panels) and blue (right panels) GC populations. Full lines show medians, the shading extends between the 5 and 95% quantiles of the distribution. Top and bottom row are for different assembly histories, as in Fig. 7. For comparison, panels also display the anisotropy profiles of the sub-populations defined by virial mass ratio, as in Fig. 8.

sub-population contributed by high VMR satellites shows very mild radial anisotropy in the central regions, to increase to  $\beta(< 20 \text{ kpc}) \sim 0.5$  for intermediate VMRs, and then quickly decrease for the subpopulation with the lowest VMR. Although the scatter is considerable, we find that the superposition of GCs cosmologically accreted from satellites with  $\log M_{\text{sat}}/M_{\text{host}} < -1.9$  is approximately isotropic at  $r \sim 40$  kpc and *tangentially biased* at smaller radii. Values of the anisotropy that are as low as  $\beta \sim -0.5$  are within the 5% quantile. Note, however, that this tangential bias is shared by only a very small fraction of the GCs in this sub-population: as mentioned in Sect. 4.1, the half-count radius of the GCs accreted from satellites with  $\log M_{\text{sat}}/M_{\text{host}} < -1.9$  is  $R_h > 135$  kpc in 90% of cases. Only a fraction of 8% is at  $R < 40$  kpc. While tangential anisotropies are not uncommon in the very central regions for the sub-population contributed by minor mergers, this is not predicted to be a dominant behaviour.

Figure 9 shows the anisotropy profiles of the full populations of red (left panels) and blue GCs (right panels). Full lines show medians, the shading extends between the 5 and 95% quantiles of the distribution. As in Fig. 7, the top row collects the 100 assembly histories in which the fractional contribution to the blue GC population of satellites with  $\log M_{\text{sat}}/M_{\text{host}} > -0.7$  is  $< 0.21$ . The bottom row has the complementary set with  $f(\log M_{\text{sat}}/M_{\text{host}} > -0.7) \geq 0.21$ . The median anisotropy of the GC sub-populations defined by VMR are also shown, for comparison, with the same colour-coding as in Fig. 8. We find that both red and blue GC populations have predominantly radial anisotropy, and that any dependence on the assembly history is minor. For

all practical purposes, red and blue populations have the same anisotropy profile:  $\beta$  is very mildly positive in the central regions ( $r \lesssim 10$  kpc), and then displays a sustained increase towards larger radii, with little scatter across different assembly histories. The anisotropy profiles of the full red and blue population can be seen to follow the profile of the sub-population with the highest VMR in the centre, and of the population with the lowest VMR in the outermost regions, where they respectively dominate. Not enough GCs contributed by satellites with  $\log M_{\text{sat}}/M_{\text{host}} < -1.9$  appear to be present in the very central regions to result in a tangentially biased orbital structure.

## 5 DISCUSSION AND CONCLUSIONS

In this paper we have investigated the kinematical properties of the GC populations assembled through hierarchical merging around massive galaxies. Our set up is purposely simplistic, and only accounts for the following fundamental ingredients:  $\Lambda$ CDM assembly histories, gravitational dynamics and measured relations between GC abundances and dark matter halo mass. This is instrumental to highlighting the possible need for any additional physical processes that are not accounted for in this work.

The ingredients above imply that the halo populations of accreted GCs have systematically different progenitors with respect to the stellar halo. This is due to the very different proportions with which accreted satellites contribute stars and GCs per unit of contributed dark matter. Because of the steepness of the SHMR, the stellar halo is dominated by the contributions of satellites with high VMR, which are strongly affected by dynamical friction. In contrast, if GC abundances are indeed approximately proportional to halo mass, minor mergers are substantially more important in building up the GC halo populations. Since the material deposited by minor mergers has different kinematic properties from the one contributed by satellites with high VMR, the accreted GC populations do not in general trace the stellar halo. However, in hosts with  $\log M_{\text{host}}(z=0)/M_{\odot} = 13.5$ , approximately 65% of material in the stellar halo and in the accreted population of red GCs have been deposited by satellites with similar distributions of VMRs. This makes red GCs a better tracer of the stellar halo. In turn, the contributions to the accreted population of blue GCs are systematically biased towards satellites with lower VMRs. In 75% of  $\Lambda$ CDM assembly histories, the fraction of the accreted population of blue GCs contributed by satellites with  $M_{\text{sat}}/M_{\text{host}} < 1/50$  at accretion is  $> 39\%$  ( $> 30\%$ ) for galaxies hosted by haloes with  $\log M_{\text{host}}(z=0)/M_{\odot} = 13.5$  ( $\log M_{\text{host}}(z=0)/M_{\odot} = 12.3$ ).

With respect to the accreted stellar halo, the fingerprints of the increased importance of minor mergers are: i) a more extended spatial distribution and ii) an increased degree of tangential motion. Even between red and blue GCs, differences in the relation between halo mass and GC abundance are sufficient to make the spatial distribution of blue GCs systematically more extended than the one of red GCs, as well as to make the velocity dispersion of the former systematically higher. The increased degree of tangential motion makes LOSVDs with negative kurtosis a distinctive trait of the increased contribution of satellites with

low VMRs. The kurtosis profiles of our toy-model accreted GC populations qualitatively reproduce those of real galaxies (e.g., Pota et al. 2013):  $\kappa \lesssim 0$  in the central regions ( $R < 40$  kpc) for both blue and red GCs;  $\kappa > 0$  at larger radii, with values that depend on the assembly history.

Negative values of the kurtosis, however, do not correspond to tangentially biased orbital distributions. The cosmologically accreted populations of GCs constructed using our set of simplifying hypotheses have anisotropy profiles that increase from mildly radial in the central regions ( $\beta(r < 10$  kpc)  $\sim 0.2$ ) to strongly radially anisotropic at large radii ( $\beta(r > 30$  kpc)  $\gtrsim 0.6$ ).

The correspondence between kurtosis and anisotropy is known to be only qualitative (e.g., Gerhard 1993; van der Marel & Franx 1993). Here we have provided an example of an equilibrium population with  $\kappa < 0$  at some radii, but  $\beta \gtrsim 0$ . We attribute this to the phase space properties of the material accreted from minor mergers, which is highly clumpy in the space of the integrals of the motion (see also NA17). We find that the sub-population of cosmologically accreted GCs with VMR  $\log M_{\text{sat}}/M_{\text{host}} < -1.9$  is tangentially biased at radii  $r \lesssim 40$  kpc, where GCs are mainly approaching the pericenter of the cosmological infall orbits of their progenitor satellites. Values of  $\beta$  can be as low as  $\sim -0.5$ . However, at these radii, the contribution of satellites with higher virial mass ratios is dominant in our models, and in fact drives the anisotropy of the full GC population.

### 5.1 Comparison with dynamical analyses

Measuring the orbital structure of pressure supported systems is a notoriously difficult task, due to strong model degeneracies. The infamous degeneracy between mass and anisotropy makes it difficult to disentangle the orbital structure of the tracer population from the profile of the embedding gravitational potential, as well as from the details of density profile of the tracers themselves (see e.g., Gerhard 1993; Binney & Tremaine 2008; Evans et al. 2009; Mamon et al. 2013, and references therein). Use of the higher moments of the LOSVD is helpful, though not always possible in dynamical analyses of GC populations, due to the limited number of available tracers (see e.g., Amorisco & Evans 2012). Literature results on the orbital structure of GC populations are mixed (see e.g., Agnello et al. 2014; Napolitano et al. 2014; Zhu et al. 2014, 2016; Zhang et al. 2015; Pota et al. 2015; Oldham & Auger 2016; Wasserman et al. 2017). Additionally, a direct comparison with our results is not straightforward as many analyses have adopted models with radially constant orbital structure. It is unclear whether a constant value of  $\beta$  may correctly describe our model populations, and what value of  $\beta$  would be inferred as a result. However, some studies have inferred a strong tangential orbital bias, which, despite these possible biases, appears difficult to reconcile with our simple toy models.

There is a number of mechanisms that may possibly be responsible for this discrepancy. For instance, the following two physical processes, which we have not accounted for, may alter the kinematics of the GC populations in the central regions of the host. First and foremost, we have neglected the contribution of GCs formed within the host halo itself, or formed during mergers (e.g., Kruijssen et al. 2012) rather than simply accreted. These may be dominant in the

central regions and our model can not predict their kinematics. For instance, the orbital distribution of material formed *in situ* is usually less radially biased than the one of material that is cosmologically accreted (e.g., Röttgers et al. 2014). Additionally, these GCs may display disk kinematics, as seen in M31 (e.g., Caldwell & Romanowsky 2016), mimicking a tangentially biased orbital structure.

Second, we have ignored the possibility that some GCs may have been shredded by the tides after they are accreted onto the host. GCs that reach closer to the centre are more easily disrupted, so that, as discussed in a number of works (e.g., Bahcall & Wolf 1976; Pota et al. 2013; Agnello et al. 2014; Wasserman et al. 2017), GC disruption may cause a systematic depletion of GCs on radial orbits, possibly altering the orbital distribution. It remains however unclear whether this effect may reconcile the present discrepancy. GC disruption is certainly a relevant process for low mass GCs (e.g., Gnedin & Ostriker 1997; Baumgardt 1998; Vesperini & Heggie 1997; Vesperini et al. 2003; Peng et al. 2008; Georgiev et al. 2010; Kruijssen et al. 2012; Gnedin et al. 2014; Mieske et al. 2014), but the accreted populations considered here only include those GCs that may survive in the contributing satellites to  $z = 0$ . Observations in the MW suggest that some GCs that likely have an accretion origin may indeed experience tidal disruption (e.g., Odenkirchen et al. 2003; Grillmair & Dionatos 2006), but we also note that our model does not clearly overestimate the hosts' expected GC abundances. This would suggest that the fraction of GCs destined to disruption *after accretion* is not substantial in our populations, as tides within the progenitor satellites have already processed the contributed GCs. This is supported by recent numerical simulations, which find that tides are in fact stronger in low mass hosts than are in massive galaxies (Brockamp et al. 2014; Zonoozi et al. 2016).

Both of these mechanisms, however, are more effective in the central regions of the host, and most likely can not significantly alter the strong radial bias that our model populations display at large radii. Therefore, observations of any signal for a tangential anisotropy at large galactocentric radii are especially interesting. These naturally raise the question of whether this behavior may be reproduced in a  $\Lambda$ CDM scenario, perhaps by relaxing some of the hypotheses made here. For example, in these models we have used that most cosmological accretion events have intermediate circularity at accretion ( $j \sim 0.5$ ), and that this is approximately independent of mass ratio (e.g. Benson 2005; Wetzel 2011; Jiang et al. 2015). As the material contributed by minor mergers best preserve memory of their infall orbit, the observed signal for tangential orbits may suggest differences in the orbital distribution at infall. In future work, it would therefore be interesting to explore whether a bias towards higher circularities for minor mergers may in fact produce accreted GC populations that are less radially biased at large radii, or even tangentially biased.

To conclude, many fundamental properties of the kinematics of GC populations around massive galaxies appear to be simply interpreted as a direct consequence of the important role of minor mergers. In particular, we have shown that there is no contradiction between the accretion scenario and the observed negative values of the kurtosis, which are instead ubiquitous when accretion events with low VMRs

are important. It will be interesting to compare the results of this work with those of future kinematical analyses.

## ACKNOWLEDGEMENTS

It is a pleasure to thank Jean Brodie, Duncan Forbes, Eric Peng and the Santa Cruz SAGES group for stimulating discussions.

## REFERENCES

- Abadi, M. G., Navarro, J. F., & Steinmetz, M. 2006, MNRAS, 365, 747
- Agnello, A., Evans, N. W., Romanowsky, A. J., & Brodie, J. P. 2014, MNRAS, 442, 3299
- Amorisco, N. C., & Evans, N. W. 2012, MNRAS, 424, 1899
- Amorisco, N. C. 2017a, MNRAS, 469, L48
- Amorisco, N. C. 2017b, MNRAS, 464, 2882
- Bahcall, J. N., & Wolf, R. A. 1976, ApJ, 209, 214
- Bailin, J., Bell, E. F., Valluri, M., et al. 2014, ApJ, 783, 95
- Baumgardt, H. 1998, AA, 330, 480
- Benson, A. J. 2005, MNRAS, 358, 551
- Behroozi, P. S., Wechsler, R. H., & Conroy, C. 2013, ApJ, 770, 57
- Bertin, G., Leeuw, F., Pegoraro, F., & Rubini, F. 1997, AA, 321, 703
- Binney, J., & Tremaine, S. 2008, Galactic Dynamics: Second Edition, by James Binney and Scott Tremaine. ISBN 978-0-691-13026-2 (HB). Published by Princeton University Press, Princeton, NJ USA, 2008.,
- Blakeslee, J. P., Tonry, J. L., & Metzger, M. R. 1997, AJ, 114, 482
- Boylan-Kolchin, M. 2017, MNRAS, 472, 3120
- Brockamp, M., Küpper, A. H. W., Thies, I., Baumgardt, H., & Kroupa, P. 2014, MNRAS, 441, 150
- Brodie, J. P., & Strader, J. 2006, ARAA, 44, 193
- Brodie, J. P., Usher, C., Conroy, C., et al. 2012, ApJL, 759, L33
- Brodie, J. P., Romanowsky, A. J., Strader, J., et al. 2014, ApJ, 796, 52
- Bullock, J. S., Kravtsov, A. V., & Weinberg, D. H. 2001, ApJ, 548, 33
- Bullock, J. S., & Johnston, K. V. 2005, ApJ, 635, 931
- Caldwell, N., & Romanowsky, A. J. 2016, ApJ, 824, 42
- Carollo, C. M., de Zeeuw, P. T., & van der Marel, R. P. 1995, MNRAS, 276,
- Cooper, A. P., Cole, S., Frenk, C. S., et al. 2010, MNRAS, 406, 744
- Cooper, A. P., D'Souza, R., Kauffmann, G., et al. 2013, MNRAS, 434, 3348
- Cooper, A. P., Cole, S., Frenk, C. S., Le Bret, T., & Pontzen, A. 2017, MNRAS, 469, 1691
- Côté, P., Marzke, R. O., & West, M. J. 1998, ApJ, 501, 554
- Deason, A. J., Mao, Y.-Y., & Wechsler, R. H. 2016, ApJ, 821, 5
- Dekel, A., Stoehr, F., Mamon, G. A., et al. 2005, Nat, 437, 707
- Evans, N. W., An, J., & Walker, M. G. 2009, MNRAS, 393, L50
- Fakhouri, O., Ma, C.-P., & Boylan-Kolchin, M. 2010, MNRAS, 406, 2267
- Forbes, D. A., Brodie, J. P., & Grillmair, C. J. 1997, AJ, 113, 1652
- Forbes, D. A., Alabi, A., Romanowsky, A. J., et al. 2016, MNRAS, 458, L44
- Forbes, D. A., Alabi, A., Brodie, J. P., et al. 2017, AJ, 153, 114
- Forbes, D. A. 2017, MNRAS, 472, L104
- Gao, L., Navarro, J. F., Cole, S., et al. 2008, MNRAS, 387, 536

- Garrison-Kimmel, S., Boylan-Kolchin, M., Bullock, J. S., & Lee, K. 2014, *MNRAS*, 438, 2578
- Garrison-Kimmel, S., Bullock, J. S., Boylan-Kolchin, M., & Bardwell, E. 2017, *MNRAS*, 464, 3108
- Georgiev, I. Y., Puzia, T. H., Goudfrooij, P., & Hilker, M. 2010, *MNRAS*, 406, 1967
- Gerhard, O. E. 1991, *MNRAS*, 250, 812
- Gerhard, O. E. 1993, *MNRAS*, 265, 213
- Gnedin, O. Y., & Ostriker, J. P. 1997, *ApJ*, 474, 223
- Gnedin, O. Y., Ostriker, J. P., & Tremaine, S. 2014, *ApJ*, 785, 71
- Grillmair, C. J., Freeman, K. C., Bicknell, G. V., et al. 1994, *ApJL*, 422, L9
- Grillmair, C. J., & Dionatos, O. 2006, *ApJL*, 643, L17
- Guo, Q., White, S., Li, C., & Boylan-Kolchin, M. 2010, *MNRAS*, 404, 1111
- Harris, W. E., Harris, G. L. H., & Alessi, M. 2013, *ApJ*, 772, 82
- Harris, W. E., Harris, G. L., & Hudson, M. J. 2015, *ApJ*, 806, 36
- Harris, W. E., Blakeslee, J. P., & Harris, G. L. H. 2017, *ApJ*, 836, 67
- Hudson, M. J., Harris, G. L., & Harris, W. E. 2014, *ApJL*, 787, L5
- Hudson, M. J., & Robison, B. 2017, *arXiv:1707.02609*
- Jethwa, P., Erkal, D., & Belokurov, V. 2018, *MNRAS*, 473, 2060
- Jiang, L., Cole, S., Sawala, T., & Frenk, C. S. 2015, *MNRAS*, 448, 1674
- Kravtsov, A. V., & Gnedin, O. Y. 2005, *ApJ*, 623, 650
- Kruijssen, J. M. D., Pelupessy, F. I., Lamers, H. J. G. L. M., et al. 2012, *MNRAS*, 421, 1927
- Li, H., & Gnedin, O. Y. 2014, *ApJ*, 796, 10
- Ludlow, A. D., Navarro, J. F., Angulo, R. E., et al. 2014, *MNRAS*, 441, 378
- Mamon, G. A., Biviano, A., & Boué, G. 2013, *MNRAS*, 429, 3079
- Mieske, S., Küpper, A. H. W., & Brockamp, M. 2014, *AA*, 565, L6
- Mistani, P. A., Sales, L. V., Pillepich, A., et al. 2016, *MNRAS*, 455, 2323
- Moody, C. E., Romanowsky, A. J., Cox, T. J., Novak, G. S., & Primack, J. R. 2014, *MNRAS*, 444, 1475
- Moore, B., Diemand, J., Madau, P., Zemp, M., & Stadel, J. 2006, *MNRAS*, 368, 563
- Moster, B. P., Somerville, R. S., Maulbetsch, C., et al. 2010, *ApJ*, 710, 903
- Naab, T., Johansson, P. H., Ostriker, J. P., & Efstathiou, G. 2007, *ApJ*, 658, 710
- Napolitano, N. R., Pota, V., Romanowsky, A. J., et al. 2014, *MNRAS*, 439, 659
- Navarro, J. F., Frenk, C. S., & White, S. D. M. 1997, *ApJ*, 490, 493
- Odenkirchen, M., Grebel, E. K., Dehnen, W., et al. 2003, *AJ*, 126, 2385
- Oldham, L. J., & Auger, M. W. 2016, *MNRAS*, 457, 421
- Oñorbe, J., Domínguez-Tenreiro, R., Sáiz, A., & Serna, A. 2007, *MNRAS*, 376, 39
- Peebles, P. J. E. 1984, *ApJ*, 277, 470
- Peng, E. W., Jordán, A., Côté, P., et al. 2008, *ApJ*, 681, 197-224
- Pillepich, A., Vogelsberger, M., Deason, A., et al. 2014, *MNRAS*, 444, 237
- Pota, V., Forbes, D. A., Romanowsky, A. J., et al. 2013, *MNRAS*, 428, 389
- Pota, V., Romanowsky, A. J., Brodie, J. P., et al. 2015, *MNRAS*, 450, 3345
- Purcell, C. W., Bullock, J. S., & Zentner, A. R. 2007, *ApJ*, 666, 20
- Ramos-Almendares, F., Abadi, M. G., Muriel, H., & Coenda, V. 2017, *arXiv:1712.05410*
- Ricotti, M. 2002, *MNRAS*, 336, L33
- Rodriguez-Gomez, V., Pillepich, A., Sales, L. V., et al. 2016, *MNRAS*, 458, 2371
- Romanowsky, A. J., & Kochanek, C. S. 2001, *ApJ*, 553, 722
- Röttgers, B., Naab, T., & Oser, L. 2014, *MNRAS*, 445, 1065
- Saglia, R. P., Kronawitter, A., Gerhard, O., & Bender, R. 2000, *AJ*, 119, 153
- Sales, L. V., Navarro, J. F., Abadi, M. G., & Steinmetz, M. 2007, *MNRAS*, 379, 1464
- Schuberth, Y., Richtler, T., Hilker, M., et al. 2012, *AA*, 544, A115
- Spitler, L. R., & Forbes, D. A. 2009, *MNRAS*, 392, L1
- Strader, J., Romanowsky, A. J., Brodie, J. P., et al. 2011, *ApJS*, 197, 33
- van der Marel, R. P., & Franx, M. 1993, *ApJ*, 407, 525
- Vesperini, E., & Heggie, D. C. 1997, *MNRAS*, 289, 898
- Vesperini, E., Zepf, S. E., Kundu, A., & Ashman, K. M. 2003, *ApJ*, 593, 760
- Wasserman, A., Romanowsky, A. J., Brodie, J., et al. 2017, *arXiv:1712.01229*
- Wetzel, A. R. 2011, *MNRAS*, 412, 49
- White, S. D. M., & Frenk, C. S. 1991, *ApJ*, 379, 52
- Zepf, S. E., & Ashman, K. M. 1993, *MNRAS*, 264, 611
- Zepf, S. E., Beasley, M. A., Bridges, T. J., et al. 2000, *AJ*, 120, 2928
- Zhang, H.-X., Peng, E. W., Côté, P., et al. 2015, *ApJ*, 802, 30
- Zhu, L., Long, R. J., Mao, S., et al. 2014, *ApJ*, 792, 59
- Zhu, L., Romanowsky, A. J., van de Ven, G., et al. 2016, *MNRAS*, 462, 4001
- Zonoozi, A. H., Rabiee, M., Haghi, H., & Küpper, A. H. W. 2016, *ApJ*, 818, 58